Local delamination on heavily deformed polymer-metal interfaces

Faber, E. T.; Vellinga, W. P.; De Hosson, J.T.M.

Published in:
Journal of Materials Science

DOI:
10.1007/s10853-013-7750-6

Publication date:
2014

J Mater Sci (2014) 49:691–700
DOI 10.1007/s10853-013-7750-6

Local delamination on heavily deformed polymer–metal interfaces: evidence from microscopy

E. T. Faber · W. P. Vellinga · J. Th. M. De Hosson

Received: 13 May 2013 / Accepted: 17 September 2013 / Published online: 1 October 2013

Abstract In this work the microstructure of interfaces present in heavily bi-axially deformed polymer-coated metal is studied. Cross sections of deformed polymer-coated steel are prepared using several polishing strategies, including the use of focused ion beam, and are imaged using optical microscopy and scanning electron microscopy. We find that the interfaces show significant details right down to the smallest scale observable with the preparation techniques used of about ~ 10 nm. Local delamination events at these deformed interfaces are observed and are found to be preferentially associated with overhanging parts on the interface. Overhanging parts are frequently observed, but only below a certain length-scale on the interfaces that are otherwise found to be self-affine up to a certain correlation length. The smallest detail includes the tail of the size distribution of the overhanging features. Together this suggests that the physical mechanisms determining the formation of critical features for adhesion operate at sub-grain level as well as at grain level.

Introduction

Polymer-coated steels are competitive alternatives to traditional materials in the packaging of food industries. Steel sheets have traditionally been lacquered in numerous post-forming stages. The use of pre-coated packaging steel cuts out several production steps and may also lead to significant reduction of energy consumption, of CO_2 emission and of solid waste [1–5]. Our specific interest is in deep-drawn (drawn-and-redrawn or DRD) laminates of poly ethylene terephthalate (PET) and electrochemically chromium-coated steel for packaging. This pre-coated material is protected against corrosion by a thin (~ 10 nm) Cr film that doubles as adhesion layer. Protection against corrosion is crucial since food packaging regulations require that the material remains free from corrosion on the inside for prolonged periods of time.

The severity of corrosion has been related to the degree of plastic deformation [1, 3]. Further experimental results point a co-evolution corrosion resistance, roughness, and work of adhesion. Plastic deformation of the steel substrate is known to be accompanied by roughening of the steel–polymer interface. The self-affine characteristics of the evolving roughness on metal surfaces have been quantified [6], and their dependence on grain size, crystal system, and strain level have been reported [7, 8]. It has been quantitatively shown using peel-tests [9] that the work of adhesion between polymers and metals decreases as a result of plastic deformation of the substrate. Laser-induced delamination has lead to the same conclusion [10, 11].

Notwithstanding this evidence on the macroscopic averaged behavior of the interface during deformation, so far there has been no microscopic experimental evidence on the evolving interface structure. Therefore this paper is aimed at investigating the influence of interface roughening on polymer-metal interfaces due to bi-axial deformation in microscopic detail, and on different length scales. The main hypothesis tested in this paper, is whether or not local delamination is occurring as a result of deformation-induced roughening, and if so, whether it is related to salient aspects of the interface geometry. To this end cross-sections of pre-deformed polymer/metal laminate samples are prepared and analyzed.

E. T. Faber · W. P. Vellinga · J. Th. M. De Hosson (✉)
Department of Applied Physics, Materials Innovation Institute M2i, University of Groningen, Nijenborgh 4, 9747 AG Groningen, The Netherlands
e-mail: j.t.m.de.hosson@rug.nl

Table 1 List of symbols

ε	Strain
mer, cir	Meridional, circumferential
z, θ	Location of sample in can
r	Drawing radius of can
P, Q, R, S, T, V, W	Sample labels
L, $L(z,\theta)$	Total length of cross-sectioned interface
L_{nom}	Nominal (projected) length of cross-sectioned interface
$g(l)$	Height–height correlation function (Eq. 2)
w	RMS roughness of interface
ξ, H	Correlation length, Hurst exponent of $g(l)$
λ	Length scale of an observed phenomenon
$G(\lambda)$	Gaussian kernel of size λ, used to remove smaller details (Eq. 8)
$F(s,\lambda)$	Approximation of the shape of the measured interface (Fig. 8)
L_{OV}, L_{132}, D, X_L, X_{OV}	Characterization parameters (illustrated in Figs. 7b, 8d; Eqs. 10, 11, 12)

Each measurement has its own resolution, which is not the same as the minimum length scale of the investigated phenomena. It is of interest to define a length scale λ, to evaluate the measured phenomena as a function of length scale, to facilitate the comparison of measurements from different sources as well as to describe the dependency of measured phenomena on length scale.

Observations made with different microscopic techniques will be combined and studied at different magnifications or length-scales λ using interpolation techniques. Only geometrical characteristics will be discussed here. A summary of symbols can be found in Table 1.

Another factor that sets this paper aside is that we discuss bi-axially deformed material such as encountered in the industrially relevant DRD process.

Experimental techniques

Materials

The polymer–metal laminate studied here is a laminate of electrolytically chromium-coated steel (ECCS) with PET as previously used for corrosion susceptibility research [1]; to study effects of microstructure and heat treatments on corrosion and to study electrolyte-induced delamination [12–14]; and to show the corrosion inhibiting effect [3] of the chromium layer and the PET layer, and to test several polymer coatings' quality [4]. The pre-rolled steel substrate has a thickness of 0.225 mm and has been electrolytically coated with a Cr layer with a thickness varying between 6 and 15 nm, similar to that examined by Boelen et al. [1]. On top of this Cr-layer a chromium oxide is found, with a thickness between 0.6 and 2.5 nm, as described in earlier research [15] and similar to the ECCS used for acetic acid-induced corrosion research [16], studying the mechanics of corrosion defect growth [1] and citric-citrate corrosion studies [17]. The multi-layered PET coating has a thickness of 20 μm and was applied by co-extrusion onto both sides of the preheated substrate. The PET layer consists of three sub-layers; a glycol-functionalized PET layer (PETG) near the ECCS interface, a bulk PET layer and a PETG layer at the surface. This is one of the polymer layers examined earlier [3]. This multilayer is simply referred to as "PET" hereafter. Bonding of the PET coating to the chromium layer is assumed to be due to hydrogen bonds of chromium hydroxyl groups with ester groups in the PET.

The resulting laminate sheet is formed into a can by a number of drawing steps, with the first draw step referred to as the draw step D and subsequent draw steps as redraw steps RD; the full process is draw-and-redraw or DRD. Since we are interested in the potential delamination issues occurring in practice we have studied samples deformed in a realistic process. Up to two draw steps were used for the material discussed in this paper. The blank radius is 90 mm, die radii are 55 and 42 mm, respectively, and bend radius is 1 mm. Depending on the initial position on the sheet, the material in the sidewall of a can has experienced different amounts as well as different types of deformation.

The qualitative differences derive from a difference in the number of deformation steps. A draw step consists of a bi-axial deformation as the blank material is pulled toward the die radius, followed by a bending step and an opposed bending (straightening) step, finally followed by a tensile strain while the material is pulled down around the die which results in wall thinning. A redraw step constitutes another bending step pair, followed by a repeat of the deformations in a draw step.

Neglecting the difference between inside and outside the qualitative deformation history can be given as the number of bending step pairs, three pairs and one pair in the currently used samples as indicated in Fig. 1. The areas are separated by a witness mark, which indicates the die radius from a previous draw step. Apart from these qualitative differences, quantitative differences occur due the fact that circular strips with differing radius in the initial sheet are deformed into rings of a single final radius in the deformed material.

The quantitative aspect of this complex deformation history is approximated with the following simplifications. The thickness of the laminate is assumed to be constant throughout the can, while wall thinning and strain in the base of the cup are assumed to be insignificant. A bi-axial strain ε, representing circumferential and meridional engineering strains, is calculated based on these assumptions.

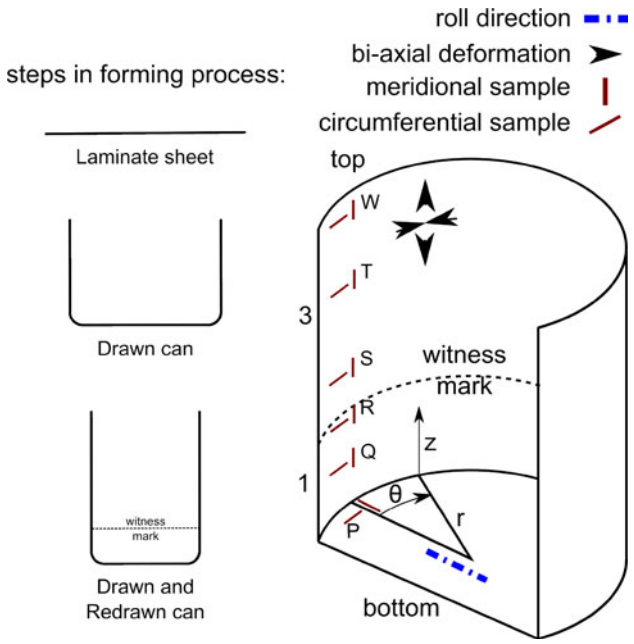

Fig. 1 Schematic of a DRD can, showing the forming steps as well as the position and orientation of samples used in this paper and of the coordinate conventions used. *Numbers* indicate number of bending step pairs (see text). *Dashed line* indicates the roll direction of the steel sheet

We define the following directions on the deformed samples (locations shown in Fig. 1): θ (circumferential), and z (meridional). This establishes a direct correspondence to our samples since we are mainly interested in the sidewalls of the cans.

For a certain drawing radius r DRD results in an meridional tensile strain $\varepsilon_{\mathrm{mer}}(z,\theta)|_{\mathrm{r}}$ and a circumferential compressive strain $\varepsilon_{\mathrm{cir}}(z,\theta)|_{\mathrm{r}}$. A dependence on the circumferential angle θ ("earing") derives from the anisotropy of the initial sheet. In this paper $\theta = 0$ for all samples and the dependence on θ is ignored.

Measured values of $\varepsilon_{\mathrm{mer}}$ and $\varepsilon_{\mathrm{cir}}$ in an comparable can are plotted in Fig. 2.

To investigate the effect of the DRD process cross sections were made in meridional and circumferential directions. In the discussion of micrographs of the circumferential cross sections we identify the direction parallel to the interface as x (macroscopic z and θ) and the direction normal to the interface as y (macroscopic r). The nominal (projected) interface length of a cross section in circumferential and meridional direction is given by

$$L_{\mathrm{nom,cir}}(z,\theta) = (1 + \varepsilon_{\mathrm{cir}}(z,\theta))L_{\mathrm{nom,cir}}(0,\theta), \quad (1a)$$

$$L_{\mathrm{nom,mer}}(z,\theta) = (1 + \varepsilon_{\mathrm{mer}}(z,\theta))L_{\mathrm{nom,mer}}(0,\theta), \quad (1b)$$

where $L_{\mathrm{nom,cir}}(0,\theta)$ and $L_{\mathrm{nom,mer}}(0,\theta)$ are reference lengths in circumferential and meridional directions, respectively, in the undeformed material (see also Fig. 4).

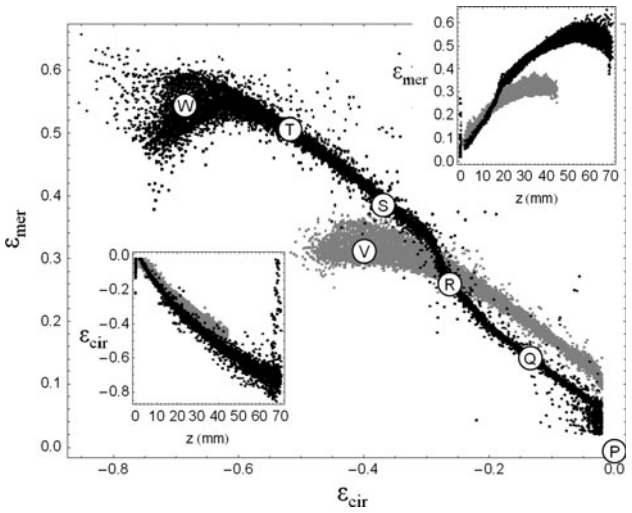

Fig. 2 Bi-axial strain of comparable DRD cans, measured with digital image correlation. The *black graph* is of a can with radius $r = 42$ mm, the *gray graph* of a can with $r = 55$ mm. Samples used in this paper are indicated on the $\varepsilon_{\mathrm{mer}}$ versus $\varepsilon_{\mathrm{cir}}$ graph. The discontinuity that can be seen in the black graph between R and S, is the witness mark that is mentioned in the text

Sample preparation

The approach pursued here is to prepare cross-sections that represent the interface geometry faithfully, i.e. without significant added damage due to preparation. The huge difference in mechanical and chemical properties of the PET and the steel is the main hurdle here since it leads to marked differences in material removal rates when using classical polishing techniques. We have used three different methods in attempts to obtain sizeable cross-sections of PET/steel interfaces and minimize the preparation damage.

Type I samples of 8 × 4 mm were cut from locations P, Q, R, S, T (Fig. 1) from a can with $r = 42$ mm, $\theta = 0$, and $z = 0$, 8, 16, 24, 40 mm. The witness mark of this can was at 17 mm. Multiple samples are stacked and mounted in a *N*,*N*-dimethyl-*P*-toluidine polymerizing matrix. Cross-sections are mechanically polished using SiC paper with incrementally smaller grit sizes, 320, 800, 1200, and 2400. The applied pressure was 8 kPa. To remove the damage introduced by the previous polishing steps the sample was subsequently polished for 16 h on a Buehler Vibromet 2 vibrational polisher, using 40 nm SiO_2 particles. Chemicals used in the polishing steps are process are water and lab-grade cleaning ethanol. These type I samples were used to examine the interface geometry on length scales from 10 μm to 5 mm using an Olympus Vanox-T reflection optical microscope operating in bright field with a 100 × NA = 0.90 objective. Images were "stitched" together if necessary using visual cues such as the interface geometry.

Type II samples R and T were subsequently etched locally by a 30 kV Ga^+ focused ion beam (FIB), with a beam current of 10–15 nA at a glancing angle of 75° with the sample normal (Fig. 3a). These samples were used to study the interface geometry on length scales between 100 nm and 100 μm using scanning electron microscopy (SEM) (Fig. 6).

Type III samples P (undeformed), V ($r = 55$ mm, $z = 40$ mm, $\theta = 0$) and W ($r = 42$ mm, $z = 70$, $\theta = 0$) were cut and mounted plan-view using silver paste as shown in Fig. 3b. 10–15 μm of the top layer of PET is removed by a Gatan dimple grinder. A thin layer of Pt was sputtered on the PET surface for conductivity. Subsequently FIB along the sample normal and the interface normal was used to expose the interface. Type III samples were used to examine the geometry of the interface with SEM (Fig. 6). The acceleration voltage of the electron beam was limited to 5 kV, since a 10 kV beam was found to cause delamination at the interface.

The rate at which FIB removes material is proportional to the probe current, and also depends on beam parameters (acceleration voltage, defocus), substrate material, and angle of incidence. A typical rate for PET is 4 $\mu m^3\ s^{-1}$ with a 10 nA beam current, which means that the extent of the interface that can be analyzed this way is rather limited.

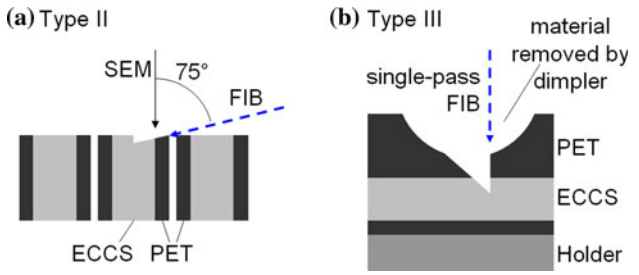

Fig. 3 Preparation method for type II (*a*) and type III (*b*) samples. **a** A pre-polished type I sample is milled by FIB at a glancing angle. **b** An unprepared laminate is mounted plan-view. 10–15 μm PET is removed by a dimpler and the interface is exposed by FIB

Results

Evolving roughness

We studied the samples as described in "Experimental techniques" section. Images were binarized using a threshold value between the brightness levels of the PET and the ECCS. Edge pixels were selected using Canny edge detection and a Hilditch morphological thinning algorithm. The set of interface pixels F defined in this way are parameterized as a curve $F(s)$. Figure 4 shows the measured interface profiles along circumferential and meridional cuts.

From the results shown in Fig. 4, we derived statistical parameters describing the self-affine interface geometry of the roughened interfaces. In statistical descriptions of the roughness, study of the influence of different length scales is usually accomplished by introducing a height-difference correlation function.

$$g\left(\vec{l}\right) = \left\langle \left[y\left(\vec{x}+\vec{l}\right) - y(\vec{x}) \right]^2 \right\rangle, \tag{2}$$

where $y(\vec{x})$ is the height at position $\vec{x}$. This definition is used in the following as well. In cases with multiple y-values for one x-value, the highest y-value was selected. Most rough surfaces are self-affine below a certain characteristic length in which case $g\left(\vec{l}\right)$ can be fit using three parameters: the root-mean-square roughness w, a correlation length ξ, and a Hurst exponent H. As predicted by Zhao et al. [18] and later confirmed by Wouters et al. [8] for Al–Mg alloys and [9] for polymer-coated steel, one finds for $l \gg \xi$:

$$g\left(\vec{l}\right) = 2w^2, \tag{3}$$

where

$$w = \sqrt{\left\langle (h - \langle h \rangle)^2 \right\rangle} \tag{4}$$

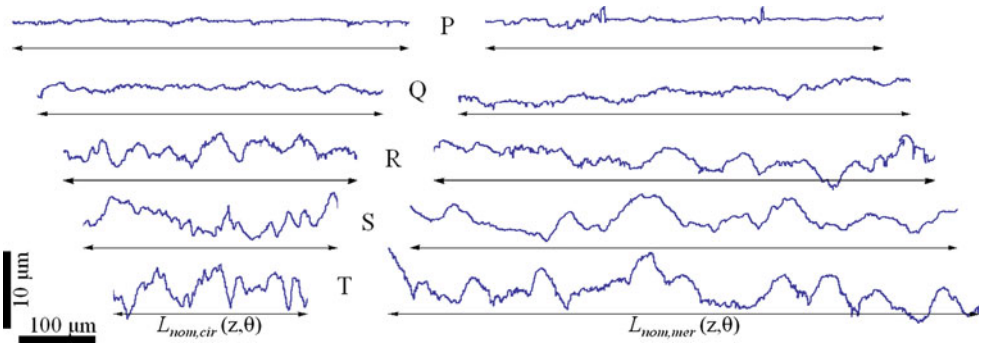

Fig. 4 Interface profiles along circumferential and meridional cuts of samples P, Q, R, S, T. Macroscopic deformation is used to calculate a projected interface length $L_{nom}(z,\theta)$ from the initial projected length $L_{nom}(0,\theta)$. The shown lengths for samples Q, R, S, and T illustrate the deformation with respect to sample P, the actual measured projected length for all samples is ~1 mm

and for $|l| \ll \xi$:

$$g\left(\vec{l}\right) = mr^{2H}. \quad (5)$$

Table 2 and Fig. 5 show the observed evolution of $g\left(\vec{l}\right)$ and the statistical roughness parameters w, ξ and H with increasing biaxial strain ε.

A number of observations can be made. It is clear that w increases with increasing ε. This is in line with earlier reports on roughening in uniaxial tension, where people observed this for tensile strained aluminum, iron, and zinc samples [7, 8]; and in 2006 even found a linear relationship for $dw/d\varepsilon$ versus grain size, while the same was observed for tensile strained steel [9] and confirmed for DRD strained steel [1]. It is also clear that the initial roughness due to the rolling ($w = 0.32 \pm 0.1$ for $\varepsilon = 0$) is dominated at later stages by intrinsic roughness due to plastic deformation mechanisms ($w_{cir} = 1.6 \pm 0.4$ and $w_{mer} = 1.8 \pm 0.4$ for $\varepsilon_{cir} = -51 \pm 5$ % and $\varepsilon_{mer} = 49 \pm 5$ %).

In the following, we assume that the other statistical properties measured at the later stages (samples R, S, T) are also representative for the intrinsic roughening, and the discussion will only refer to those samples.

The correlation length ξ is associated with the correlation between available slip systems and was found to be equal to the grain size for non-textured metals in uniaxial tension [7]. ξ in the tensile direction has also been found to scale with strain in uniaxial tension [9]. For initially rough and textured material such clear correlations with the microstructure can perhaps not be expected and in any case a study of the behavior of ξ should be combined with orientation imaging microscopy which is beyond of the scope of this paper. Here we find $\xi_{cir} < \xi_{mer}$, which seems reasonable considering the circumferential direction is associated with compression and the meridional direction with tension. In fact, based on an equiaxed starting situation and proportional scaling of ξ, one would expect $\xi_{cir}/\xi_{mer} = 0.49/1.49 = 0.33$. This compares well to the ratio encountered in the experiment ($\xi_{cir}/\xi_{mer} = 0.33$). Taking this as a base value and extrapolating to ξ values at zero strain we find that at $\varepsilon = 0$, $\xi_{cir} = 16.3$ μm, and $\xi_{mer} = 16.1$ μm, which is of the same order of magnitude as the grain size for the samples determined by OIM (13.7 and 14.7 μm, respectively).

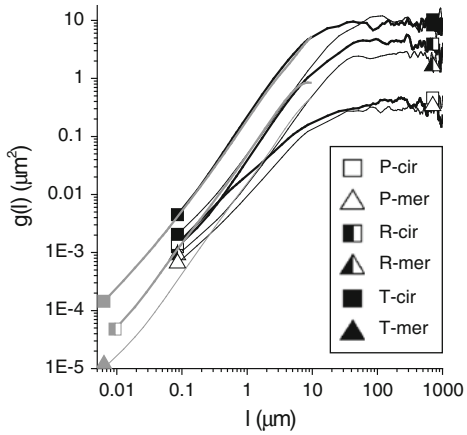

Fig. 5 $g(l)$ for samples P, R, and T along meridional (*thin line*) and circumferential (*thick line*) cross sections. *Black lines* results from optical microscopy. *Gray lines* results from SEM microscopy

Focusing again on the highly deformed samples R, S, and T we find that for the Hurst exponents $H_{cir} \approx H_{mer} \approx 0.8$, which is comparable to values found for Fe in research by Wouters et al. [7]. This means the circumferential interface profile is similar to the meridional profile, but compressed on all length scales in the x-direction by a factor ξ_{mer}/ξ_{cir}. Indeed for $l < \xi$, $g(l)$ is higher in circumferential than in meridional cross-sections, i.e. short-range height differences are more pronounced in the circumferential direction.

Local delamination

More importantly we studied local phenomena that have not been directly observed in previous research: overhanging features and instances of local delamination. Examples are shown in Fig. 6.

At low strains and at low magnification the circumferential interface profiles show a gentle wavy shape. At high strains and at high magnifications this shape locally develops into profiles like the one shown in Fig. 6 (top). Locally this interface shows a number of dramatic features (Fig. 6, bottom) where it doubles back on itself, forming

Table 2 Statistical roughness parameters w, ξ, H for samples P, Q, R, S and T

	ε_{cir} (%)	w_{cir} (μm)	ξ_{cir} (μm)	H_{cir}	ε_{mer} (%)	w_{mer} (μm)	ξ_{mer} (μm)	H_{mer}
P	0	0.32 ± 0.1	9.6 ± 2	0.49 ± 0.05	0	0.32 ± 0.1	12 ± 3	0.62 ± 0.03
Q	−13 ± 2	0.6 ± 0.2	13 ± 5	0.64 ± 0.08	14 ± 2	0.6 ± 0.2	21 ± 5	0.70 ± 0.07
R	−26 ± 3	1.3 ± 0.3	16 ± 5	0.81 ± 0.04	26 ± 3	0.9 ± 0.3	23 ± 6	0.75 ± 0.04
S	−36 ± 4	1.5 ± 0.3	11 ± 3	0.81 ± 0.04	38 ± 4	1.2 ± 0.3	22 ± 5	0.75 ± 0.04
T	−51 ± 5	1.6 ± 0.4	8 ± 3	0.78 ± 0.09	49 ± 5	1.8 ± 0.4	24 ± 6	0.77 ± 0.02

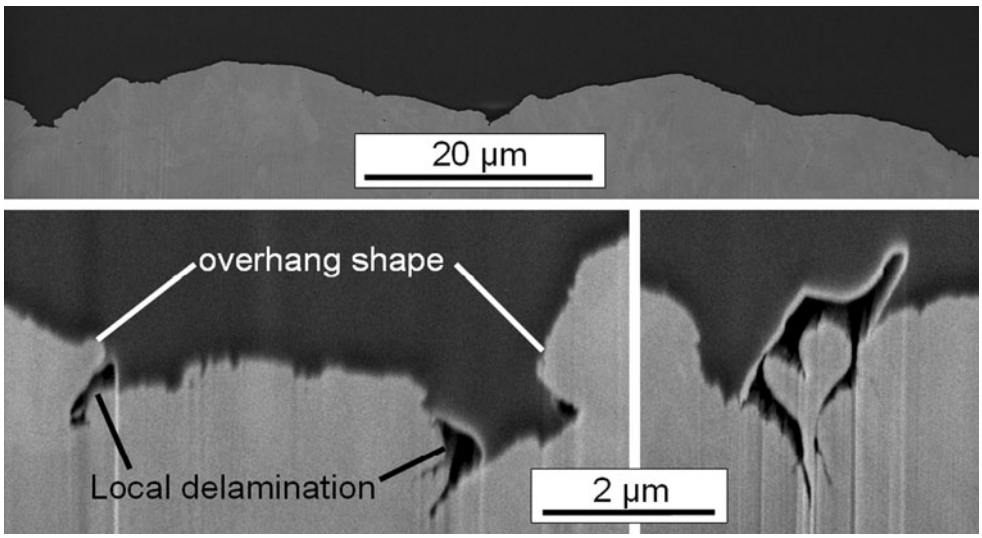

Fig. 6 Examples of local delamination and overhanging parts on deformed interfaces. *Top* sample T-cir. *Bottom* sample W-cir

overhangs. Such features will only be visible in microscopy using cross-section techniques, similar to the ones employed here, and apparently have been missed in the literature so far. In Fig. 6, local delaminated areas are also visible, showing up as dark areas located near these salient features, suggesting that the two phenomena are related.

Finally, the delamination as introduced in Fig. 6 was quantified by measuring the quantity D (defined in Fig. 7), for every delamination feature on samples P, V, and W. Delamination events were observed on samples V and W, and a cumulative plot of D is shown in Fig. 7. The most deformed sample W shows the largest cumulative delamination length, and it also shows the largest individual delamination events. Both delamination fraction and delamination size were significantly larger in circumferential direction than in meridional direction. No delamination was observed in the undeformed sample P. For a small portion of the delamination events no obvious cause is visible in terms of interface geometry. However, there appears to be an association with the previously described overhanging shapes for most of the events. Geometric properties of all the delamination events observed were studied to search for a correlation between overhanging features and delamination events.

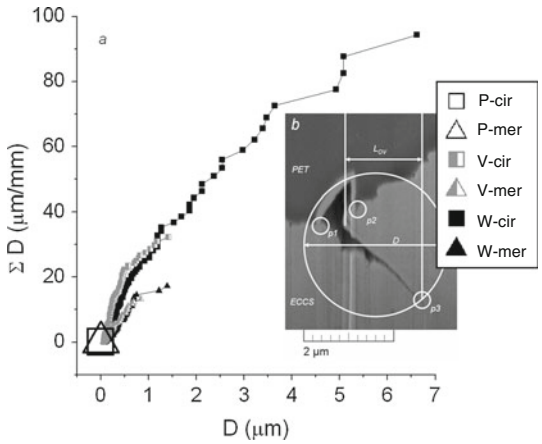

Fig. 7 **a** Cumulative size D (diameter of the smallest circle bounding delamination feature) for samples P, V, and W. For each case, the measured $L_{nom} = 1$ mm. Individual feature size and cumulative feature size are much higher for the heavily deformed W-cir. **b** Quantities measured directly from micrographs: diameter D of smallest bounding disk (used here), the width under associated overhangs L_{Ov}, PET/ECCS/vacuum triple points p1 and p2, most distant point in delaminated region p3 (used later)

Discussion

Adhesion and length scales

During DRD operations the PET is pressed into contact with the roughening and deforming steel. It has been shown that in a similar deformation procedure (Draw Wall Ironing) the PET is under high hydrostatic compressive stress [19], and that in such conditions plastic deformation modes are suppressed [20]. The constrained boundary conditions during deformation are relaxed after the process completes, and the PET is free to adapt to the changed boundary conditions at the interface.

So, in essence during deformation elastic energy is locally stored during deformation, and it is released in various dissipative processes such as plastic deformation or delamination. According to [21], delamination may occur if the locally stored energy is higher than the (also evolving) local work of adhesion and if the local stresses are sufficiently high. Considering that roughness is usually self-affine in nature it is not a priori clear which length-scale is critical for delamination, and therefore what

"local" is supposed to mean here. From studies of the relation between interface roughness, adhesion, and delamination it has been convincingly argued [22–25] that the geometry of adhering interfaces at all spatial length scales needs to be taken into account. Introducing the following equation makes that clear. The equation roughly approximates the energy needed to deform a material elastically to make complete contact with a rough interface:

$$U_{\mathrm{el}} = \int \sigma \cdot \mathrm{d}V \approx E \cdot \frac{y^2}{\lambda^2} \cdot \lambda^3 \approx E \cdot y^2 \cdot \lambda. \tag{6}$$

The simplified physical picture is that of an interface with only one relevant roughness length scale λ. On the interface volumes λ^3 are supported at contact lines with separation λ that span depressions with depth y. A uniaxial strain of the order y/λ is needed to push the material into contact with the interface. Further using E for the Young's modulus and σ for the stress leads to Eq. 6. The crucial point that follows is that U_{el} depends on λ and $y(\lambda)$. We follow Persson [23] in extending this picture to realistic interfaces in which λ now signifies the smallest detail present in a certain observation of an interface. The length scale λ may for example be related to a magnification ζ as $\zeta = L/\lambda$ with L the macroscopic size of the sample. Observing a sample at increasing ζ or "at decreasing λ", for example using different microscopic techniques may therefore have an impact on conclusions regarding the stability of the interface.

The condition that $U_{\mathrm{el}}(\lambda) > U_{\mathrm{ad}}(\lambda)$ is necessary (but not sufficient) for delamination to take place, and has been used to predict area fraction of contact for interfaces with different self-affine geometries [22–25]. Here, $U_{\mathrm{ad}}(\lambda)$ includes the effect that at smaller λ the specific interface area increases which in principle may lead to an increase of the work of adhesion. This approach takes into account the local effects in a statistical sense. This is in contrast to explicit modeling of local delamination [26, 27], where interface stresses are taken into account by using a cohesive zone description for an interface between a roughening substrate and PET.

The local predictions by such model treatments have not yet been tested in experiments. Therefore, in contrast to approaches mentioned above we start from experimentally determined interface geometries and discuss details of the geometry as well as of associated delamination events.

Analogous to the treatment in [22–25] as explained above, the interface geometry is analyzed separately on multiple length scales, in other words at different magnifications.

Observation at length scale λ, is then defined as an observation on a dataset of which F has been convolved with a discrete Gaussian kernel $G(\lambda)$ as follows:

$$F(\lambda) = G(\lambda) * F, \tag{7}$$

with $G(\lambda)$

$$G(\lambda) = [g_{-3l_{\mathrm{G}}}, g_{-3l_{\mathrm{G}}+1}, \ldots, g_{3l_{\mathrm{G}}}],$$
$$\text{where } g_n = \frac{e^{-\left(\frac{n}{l_{\mathrm{G}}}\right)^2}}{\sum_{n=-3l_{\mathrm{G}}}^{3l_{\mathrm{G}}} e^{-\left(\frac{n}{l_{\mathrm{G}}}\right)^2}}. \tag{8}$$

The width of the kernel in pixels l_{G} can be related to the width in meters λ using $l_{\mathrm{G}} = \frac{\lambda}{C}$, where C is the image scale in m pixel^{-1}.

Due to the nature of optical microscopy, detail below a length scale λ_{base} cannot be observed. This can be treated as if a perfect dataset F was convolved with a $G(\lambda_{\mathrm{base}})$ to obtain the measured F_{m}, before being convolved again with $G(\lambda_{\mathrm{chosen}})$. Consecutively convolving a dataset with two Gaussian kernels $G(\lambda_{\mathrm{base}})$ and $G(\lambda_{\mathrm{chosen}})$ is the same as convolving the data set a single time with a Gaussian $G(\lambda)$, where the effective λ is calculated according to Eq. 9.

$$\lambda = \sqrt{\lambda_{\mathrm{base}}^2 + \lambda_{\mathrm{chosen}}^2}. \tag{9}$$

For further analysis $F(\lambda)$ is parameterized as $F(s,\lambda)$ using splines.

Interface length

The interface length $L(\lambda)$ is defined (analogous to definition in an earlier article [23]) as the interface length when it is smooth at all scales below λ. This length was calculated for many different magnifications (and associated length scales λ) for a few samples. The parametric description $F(s,\lambda) = (x(s,\lambda),y(s,\lambda))$ (see Fig. 8) is used to describe positions along the interface. Calculating the interface length $L(\lambda,\varepsilon)$ as

$$L(\lambda,\varepsilon) = \int \sqrt{\left(\frac{\mathrm{d}x}{\mathrm{d}s}\right)^2 + \left(\frac{\mathrm{d}y}{\mathrm{d}s}\right)^2}\,\mathrm{d}s, \tag{10}$$

a relative length increase due to roughening can be defined as:

$$X_L(\lambda,\varepsilon) = \frac{L(\lambda,\varepsilon) - L_{\mathrm{nom}}(\lambda,\varepsilon)}{L_{\mathrm{nom}}(\lambda,\varepsilon)}. \tag{11}$$

Results are shown in Fig. 9. Results from optical microscopy and SEM were combined on a single axis using Eq. 9 with $\lambda_{\mathrm{base}} = 750$ nm. As is shown in Fig. 9, sample T-cir shows X_{L} up to 23 % and sample R-cir shows X_{L} up to 9 %. The increase in interface length is of course correlated with increased roughness. The values of X_{L} were found to be much higher for circumferential cross-sections than for meridional cross-sections. However, the main

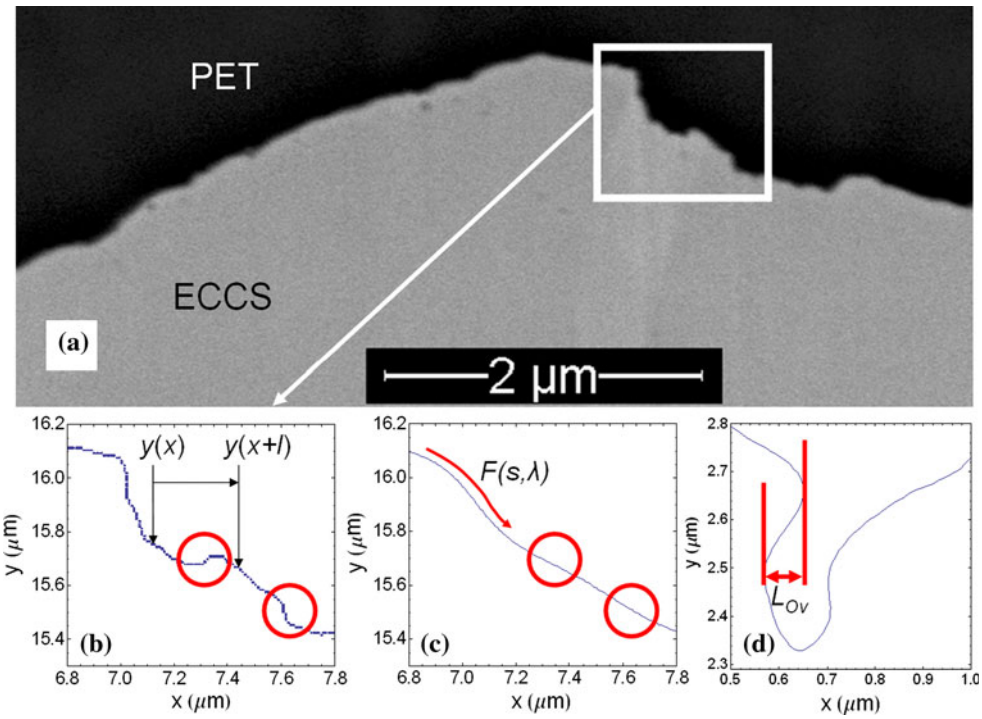

Fig. 8 Analysis of micrographs. **a** SEM image of PET/ECCS interface. **b** Interface pixels obtained by edge detection and morphological thinning. **c** Parameterized interface $F(s,\lambda)$ with $\lambda = 500$ nm (see text). **d** Definition of overhang length L_{Ov} on parametrized curve $F(s,\lambda)$

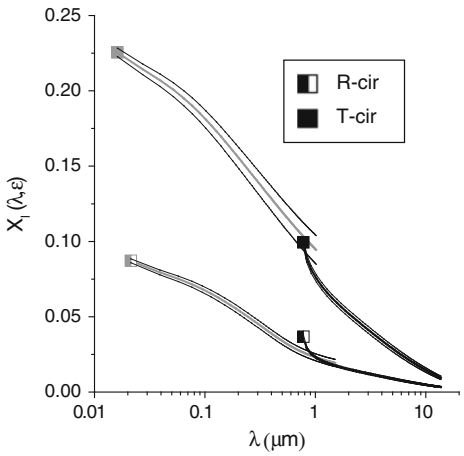

Fig. 9 X_L versus λ, calculated from $F(s,\lambda)$ for samples R and T. *Black plots* optical measurements, *gray plots* SEM measurements

point we want to illustrate here is that the X_L values show little sign of saturating right down to the smallest length scale investigated (~ 10 nm), which means that such scales cannot be excluded a priori from considerations or models concerning the evolution of adhesion at these interfaces. Usually some lower limit to the detail considered is introduced based without a clear physical justification. For example a much larger minimum size of 1 μm was used previously [26, 27] calculate X_L for uniaxially deformed samples as a function of ε.

Overhanging shapes

The projected width L_{ov} of the overhanging features was determined from $F(s,\lambda)$ as defined in Fig. 8d. The sum of all L_{ov} for each interface was used to calculate the overhang fraction $X_{OV}(\lambda,\varepsilon)$,

$$X_{OV}(\lambda,\varepsilon) = \frac{\sum L_{OV}(\lambda,\varepsilon)}{L_{nom}(\varepsilon)} \tag{12}$$

at several different values of λ.

Results are shown in Fig. 10. $X_{OV}(\lambda,\varepsilon)$ is larger for sample T-cir, the sample with the highest strain, for all length scales λ. The highest value observed for T-cir was $X_{OV}(\lambda,\varepsilon) = 1.7$ % ($\lambda = 50$ nm, $\varepsilon \approx 70$ %). This is a small number that justifies neglecting the overhangs in the calculation of $g(l)$ in the previous section. Overhangs could only be observed below a certain critical λ_c which was higher for T-cir than for R-cir: ~ 1.7 versus ~ 0.7 μm.

The hypothesis tested in this paragraph is that the areas of local delamination are spatially correlated with overhanging features. Sample W-cir (showing the largest area fraction of delamination and the largest individual delamination events) was examined in some detail to investigate this relation. For every delamination event we calculate L_{ov}, D, and the delaminated length L_{132} (see Fig. 7b).

The results are shown in Fig. 11 as cumulative number fraction and cumulative length fraction of delamination events as a function of L_{ov}. From the fact that the cumulative curves do not reach the value of 1 it is clear that part

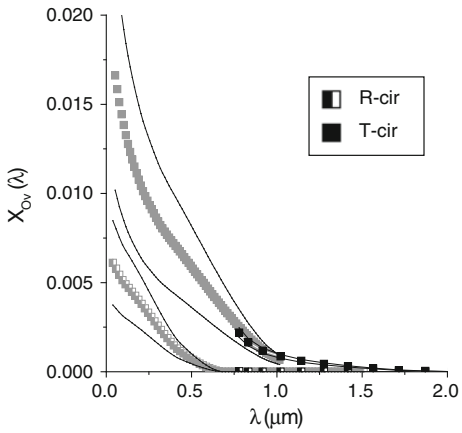

Fig. 10 X_{Ov} versus λ, calculated from $F(s,\lambda)$ for samples R and T. *Black symbols* optical microscopy. *Gray symbols* SEM

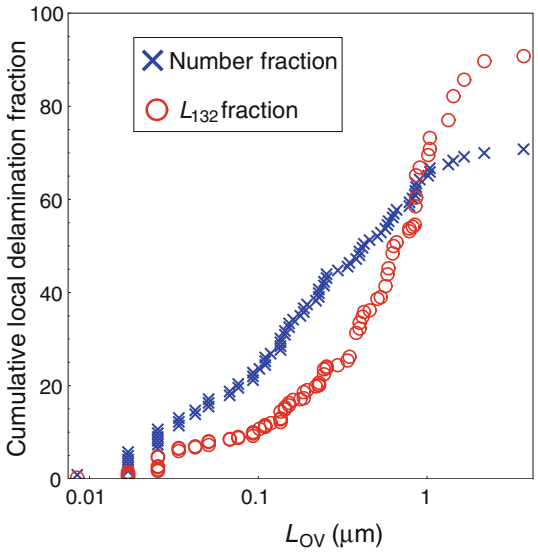

Fig. 11 Cumulative number fraction and length fraction of delamination events as a function of overhang length for sample W-cir. Total measured $L_{nom} = 1$ mm

of the delamination events is not associated with overhanging features. However, 71 % of the delamination events (by number) is associated with overhangs and in fact those events account for 91 % of the delamination length. From this we conclude that there is indeed a strong relation between the occurrence of overhang and delamination, and that the formation of these overhangs may be critical to adhesion loss. The size distribution of overhanging parts and of delaminated areas is very broad, spanning 3 decades. In fact, the smallest observable detail on these interfaces includes the tail of the size distribution of the overhanging features. This suggests that several different physical mechanisms are at play, at sub-grain, and grain level. These features could be formed in a variety of ways all associated with the compression of the interface in the circumferential direction. Folding, cracking, shearing, and extrusion are all a possibility. Two examples are shown schematically in Fig. 12. As mentioned in Evolving roughness, the strains introduced in the polymer may be an important factor in the delamination process. Delamination could be more likely to start and/or propagate where strains are high, i.e. in regions with a high interface curvature, and where the applied pressure is less effective. An appreciable curvature is necessary for all forms of overhang. Large overhanging shapes would also reduce the effective pressure applied to the local interface. Detailed orientation imaging microscopy may be needed to investigate which mechanisms play a role in the formation of these features.

Conclusions

The interface geometry of polymer–metal interfaces in biaxially deformed deformed ECCS/PET laminates has been studied by cross-sectioning samples and imaging the exposed interfaces with optical microscopy and SEM. The

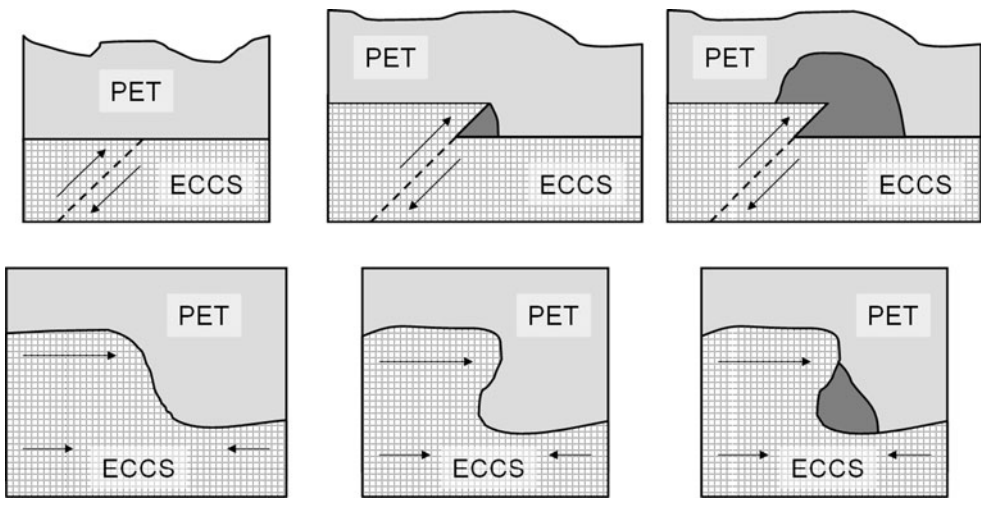

Fig. 12 Schematic depiction of sub-grain level mechanism and grain level mechanism, which may cause both overhangs and delamination. *Top* shear-induced slip creates a very small overhang and starts delamination locally, after which stresses in the PET cause the delaminated volume to grow. *Bottom* shear causes grain extrusion, increasing the curvature of the interface and straining the PET to the point that the interface delaminates

interface geometry was found to be self-affine below a correlation length ξ. Values for the Hurst exponent were in accordance with previous research. The correlation length measured in heavily deformed material along the meridional and circumferential directions was different, in accordance with the state of deformation.

Overhanging features were observed and the location of delamination events was shown to be strongly correlated with these features. Large delamination events specifically were found at large overhanging shapes. So, even though they only cover a tiny part of the interface area (<2 % for the samples studied) it is suggested that the evolution of overhanging features may be critical to the issue of adhesion and corrosion at these interfaces. Furthermore, since such overhanging features are missed in the most commonly used roughness measurement techniques it is concluded that judicious preparation of cross-sections such as attempted here is necessary for the understanding of adhesion on these interfaces.

Finally, it was concluded that the interfaces showed significant details right down to the smallest scale observable with the preparation techniques used of about $\sim$10 nm. The smallest detail includes the tail of the size distribution of the overhanging features. Together this suggests that the physical mechanisms determining the formation of critical features for adhesion operate at subgrain level as well as at grain level.

Acknowledgements This research was carried out under project number M63.7.09343 in the framework of the Research Program of the Materials Innovation Institute M2i (www.m2i.nl).

References

1. Boelen B, den Hartog H, van der Weijde H (2004) Prog Org Coat 50:40
2. Zumelzu E, Rull F, Boettcher AA (2006) J Mater Process Technol 173:34
3. Zhang X, Boelen B, Beentjes P et al (2007) Prog Org Coat 60:335
4. De Vooys A, Boelen B, Penning JP, van der Weijde H (2009) Prog Org Coat 65:30
5. Van den Bosch MJ, Schreurs PJG, Geers MGD (2009) J Mater Process Technol 209:297
6. Zaiser M, Grasset F, Koutsos V, Aifantis E (2004) Phys Rev Lett. doi:10.1103/PhysRevLett.93.195507
7. Wouters O, Vellinga W, Van Tijum R, De Hosson JTM (2006) Acta Mater 54:2813
8. Wouters O, Vellinga W, Van Tijum R, de Hosson J (2005) Acta Mater 53:4043. doi:10.1016/j.actamat.2005.05.007
9. Van den Bosch MJ, Schreurs PJG, Geers MGD, van Maris MPFHL (2008) Mech Mater 40:302. doi:10.1016/j.mechmat.2007.09.002
10. Fedorov A, De Hosson JTM (2005) J Appl Phys 97:123510. doi:10.1063/1.1929858
11. Fedorov A, van Tijum R, Vellinga WP, De Hosson JTM (2007) J Appl Phys 101:043520. doi:10.1063/1.2434805
12. Zumelzu E, Ortega C, Rull F, Cabezas C (2011) Surf Eng 27:485. doi:10.1179/026708410X12687356948436
13. Zumelzu E, Rull F, Ortega C, Cabezas C (2009) J Appl Polym Sci 113:1853. doi:10.1002/app.30077
14. Zumelzu E, Rull F, Boettcher A (2005) Ing Quim 27:13
15. Kamm G, Wiley A, Linde N (1969) J Electrochem Soc 116:1299. doi:10.1149/1.2412305
16. Beentjes P (2004) Ph.D. Thesis, Delft University of Technology, Delft
17. Zumelzu E, Cabezas C, Delgado F (2004) J Mater Process Technol 152:384
18. Zhao, Wang, Lu (2000) Principles and Applications, vol 1st ed. Academic press, San Diego, p 277
19. Mulder J, Nagy GT, Šuštarič P et al (2010) AIP Conf Proc (USA) 1252:762
20. Rabinowitz S, Ward I, Parry JSC (1970) J Mater Sci 5:29. doi:10.1007/BF02427181
21. Xu X, Needleman A et al (1993) Model Simul Mater Sci Eng 1:111
22. Persson B (2002) Phys Rev Lett. doi:10.1103/PhysRevLett.89.245502
23. Persson BNJ (2006) Surf Sci Rep 61:201. doi:10.1016/j.surfrep.2006.04.001
24. Persson BNJ (2001) J Chem Phys 115:3840. doi:10.1063/1.1388626
25. Peressadko A, Hosoda N, Persson B (2005) Phys Rev Lett. doi:10.1103/PhysRevLett.95.124301
26. Van Tijum R, Vellinga W, De Hosson JTM (2007) Acta Mater 55:2757
27. Van Tijum R, Vellinga WP, De Hosson JTM (2007) J Mater Sci 42:3529. doi:10.1007/s10853-006-1374-z